

Article

A Novel Dual-Ion Capacitive Deionization System Design with Ultrahigh Desalination Performance

Yuxin Jiang ¹, Zhiguo Hou ², Lvji Yan ¹, Haiyin Gang ¹, Haiying Wang ^{1,3,4,*} and Liyuan Chai ^{1,3,4}¹ School of Metallurgy and Environment, Central South University, Changsha 410083, China² School of Chemistry and Materials, University of Science and Technology of China, Hefei 230026, China³ Chinese National Engineering Research Center for Control and Treatment of Heavy Metal Pollution, Changsha 410083, China⁴ Water Pollution Control Technology Key Lab. of Hunan Province, Changsha 410083, China

* Correspondence: haiyw25@csu.edu.cn

Abstract: Capacitive deionization is an emerging desalination technology with mild operation conditions and high energy efficiency. However, its application is limited due to the low deionization capacity of traditional capacitive electrodes. Herein, we report a novel dual-ion capacitive deionization system with a lithium-ion battery cathode $\text{LiMn}_2\text{O}_4/\text{C}$ and a sodium-ion battery anode $\text{NaTi}_2(\text{PO}_4)_3/\text{C}$. Lithium ions could enhance the charge transfer during CDI desalination, while $\text{NaTi}_2(\text{PO}_4)_3/\text{C}$ provided direct intercalation sites for sodium ions. The electrochemical capacities of the battery electrodes fitted well, which was favorable for the optimization of the desalination capacity. The low potential of the redox couple $\text{Ti}^{3+}/\text{Ti}^{4+}$ (-0.8 V versus Ag/AgCl) and intercalation/deintercalation behaviors of sodium ions that suppressed hydrogen evolution could enlarge the voltage window of the CDI process to 1.8 V. The novel CDI cell achieved an ultrahigh desalination capacity of $140.03 \text{ mg}\cdot\text{g}^{-1}$ at 1.8 V with an initial salinity of 20 mM, revealing a new direction for the CDI performance enhancement.



Citation: Jiang, Y.; Hou, Z.; Yan, L.; Gang, H.; Wang, H.; Chai, L. A Novel Dual-Ion Capacitive Deionization System Design with Ultrahigh Desalination Performance. *Polymers* **2022**, *14*, 4776. <https://doi.org/10.3390/polym14214776>

Academic Editor: Shuang Luo

Received: 19 October 2022

Accepted: 31 October 2022

Published: 7 November 2022

Publisher's Note: MDPI stays neutral with regard to jurisdictional claims in published maps and institutional affiliations.



Copyright: © 2022 by the authors. Licensee MDPI, Basel, Switzerland. This article is an open access article distributed under the terms and conditions of the Creative Commons Attribution (CC BY) license (<https://creativecommons.org/licenses/by/4.0/>).

Keywords: capacitive deionization; desalination; dual-ion; battery electrode

1. Introduction

Desalination is an inevitable choice for solving the global freshwater scarcity crisis, which has been a hotspot of scientific research over recent years [1–3]. A number of techniques have been put into industrial application, such as multi-effect distillation, multi-stage flash, membrane distillation, reverse osmosis, nano/ultrafiltration, etc. [4–9]. However, these methods are mainly thermal-driven or pressure-driven, which are energy-intensive. On the other hand, capacitive-deionization (CDI), as an emerging energy-efficient desalination technology that employs electrode materials to adsorb salt from saline water, could operate under mild conditions [10,11]. Moreover, energy could be stored simultaneously during desalination in CDI [12], which is a mechanism similar to a capacitor [13].

Yet, the CDI technology has already been scaled up by only a few commercial companies (EST Water and Technologies in China, Current Water Technologies in Canada, etc.) [14]. The main obstacle hindering the wide application of CDI is the low desalination capacity [15]. Traditional electrode materials in CDI are mainly carbon-based materials. These materials adsorb salt with the mechanism of electric double layers; thus, the capacity is strongly limited by the specific surface area of the carbonaceous material ($<15 \text{ mg}\cdot\text{g}^{-1}$) [16,17]. Nevertheless, battery electrode materials with larger electrochemical capacities, which could store salt ions not only on the surfaces but also in the inner crystal structures, have shown great potential in CDI desalination [18,19]. Numerous battery electrodes have been employed in CDI to obtain high desalination capacities. Lee [20] used a $\text{Na}_4\text{Mn}_9\text{O}_{18}$ electrode in a hybrid CDI (HCDI) system with activated carbon (AC) as the counter electrode, and a deionization capacity of $31.2 \text{ mg}\cdot\text{g}^{-1}$ was achieved. Ahn [21]

coupled chloride-capture electrode Ag with another battery electrode AgCl, and reached a high desalination capacity of $85 \text{ mg}\cdot\text{g}^{-1}$. Furthermore, in order to enhance the charge transfer in the CDI processes, carbon-based materials are usually incorporated into battery electrode materials. For example, Yue [22] employed $\text{Na}_4\text{Ti}_9\text{O}_{20}/\text{C}$ in an HCDI cell and reached a CDI capacity of $66.14 \text{ mg}\cdot\text{g}^{-1}$, which was nearly twice that with the pure $\text{Na}_4\text{Ti}_9\text{O}_{20}$ electrode. Moreover, it is noticeable that most of the battery electrodes utilized in CDI are mainly sodium-ion batteries or chloride-ion battery electrodes, owing to the direct relationship with the composition of the salt. Theoretically, the lithium-ion could be a more efficient charge carrier compared to these salt ions because of the smaller mass per unit of carried charge [23–26], and better desalination performance might be brought out. Based on this consideration, our group synthesized lithium-ion battery material $\text{LiMn}_2\text{O}_4/\text{C}$, which was further employed as the cathode in an HCDI device [27]. The CDI cell exhibited a superior desalination capacity of $117.3 \text{ mg}\cdot\text{g}^{-1}$ compared to other deionization performances. However, the anode material in this HCDI cell was AC, the capacity of which was far lower than that of the cathode, restricting the further enhancement of the desalination capacity of the system.

Herein, we present a novel dual-ion CDI system with a lithium-ion battery cathode and a sodium-ion battery anode. The sodium superion conductor (NASICON) material $\text{NaTi}_2(\text{PO}_4)_3/\text{C}$ was chosen as the anode material. $\text{NaTi}_2(\text{PO}_4)_3$ is a stable aqueous sodium-ion anode material that could capture sodium ions during CDI [28], and the coating of carbon could facilitate the charge transfer within the process [29]. The reversible capacity of $\text{NaTi}_2(\text{PO}_4)_3/\text{C}$ was tested to be $98.63 \text{ mAh}\cdot\text{g}^{-1}$, and beneficial for the full exploitation of the cathode capacity ($70.57 \text{ mAh}\cdot\text{g}^{-1}$). The simultaneous redox behaviors of the electrodes were studied with characterization methods. The dual-ion cell achieved an ultrahigh desalination capacity of $140.03 \text{ mg}\cdot\text{g}^{-1}$ with an initial salt concentration of 20 mM, which could open up a new window for the elevation of CDI desalination efficiency.

2. Materials and Methods

2.1. Experimental Agents

Spinel LiMn_2O_4 (LMO) was purchased from Ziyi Co., Ltd. (Shanghai, China). Anion-exchange membrane (AMX) was purchased from ASTOM Corp. (Tokyo, Japan). Polyvinylidene fluoride (PVDF, HSV900) was purchased from MTI Corp. (Richmond, CA, USA). Carbon black was purchased from Cabot Corp. (Boston, MA, USA). N-Methylpyrrolidone (NMP, 99%) and polytetrafluoroethylene preparation (PTFE, 60%) was purchased from Aladdin Corp. NaCl ($\geq 99.8\%$), LiCl (analytical grade) and glucose (analytical grade) were purchased from Sinopharm Group. (Beijing, China). NaH_2PO_4 (99%), $\text{NH}_4\text{H}_2\text{PO}_4$ (99%), and TiO_2 (99%) were purchased from Macklin Co., Ltd. (Shanghai, China). Hydrophilic carbon paper was purchased from TORAY Industries, Inc., titanium plates were purchased from Rulin Co, Ltd. (Changsha, China), and titanium mesh was purchased from Kangwei Co., Ltd. (Hengshui, China). AC was purchased from Nanjing XFNANO Materials Tech Co., Ltd. (Nanjing, China).

2.2. Preparation of Materials

The $\text{LiMn}_2\text{O}_4/\text{C}$ composites were prepared with a simple ball-milling method according to our previous study [25], spinel LMO and carbon black were mixed with a mass ratio of 2:1 and then milled in a ball mill (YXQM-4L, MITR) for 6 h.

$\text{NaTi}_2(\text{PO}_4)_3/\text{C}$ was synthesized by a hydrothermal–spraying–calcination method [30]. Stoichiometric amounts of NaH_2PO_4 , $\text{NH}_4\text{H}_2\text{PO}_4$, and TiO_2 were used in a hydrothermal process at 150°C to produce the precursor of the material. Glucose was then mixed with the precursor and the composites were sprayed and annealed at 700°C in N_2 afterwards.

2.3. Characterization

Field-emission scanning electron microscope (FESEM, JSM-7900F, JEOL) and transmission electron microscope (TEM, Titan G2 60-300 with image corrector, FEI) were used to

observe the structures of the materials. Energy dispersion spectroscopy (EDS, Octane Elect Super, EDAX) was used to study the element dispersion of the material. X-ray diffraction (XRD, Empyrean 2, PANalytical) and X-ray photoelectron spectroscopy (XPS) were used to obtain information on structures and valences in the composites. Infrared carbon and sulfur analyzer (CS844, LECO) was used to measure the carbon content in the prepared material. The Brunauer–Emmett–Teller (BET) tests were carried out with the surface area and pore size analyzer (KUBOX1000, Bjbuilder).

2.4. Fabrication of Electrodes

As for the fabrication of $\text{LiMn}_2\text{O}_4/\text{C}$ electrode or AC electrode, active material, carbon black, and PVDF were ground with a mass ratio of 8:1:1 to obtain a homogeneous mixture that was further mixed with NMP for another 5 min to form a slurry. It was then painted onto the surface of carbon paper for the electrochemical test or titanium plate for the CDI test. Afterwards, the current collectors were kept at the temperature of $90\text{ }^\circ\text{C}$ for 4 h to complete the electrode preparation.

The fabrication of the $\text{NaTi}_2(\text{PO}_4)_3/\text{C}$ electrode was basically similar to that of the $\text{LiMn}_2\text{O}_4/\text{C}$ electrode, however, there were some differences. The binder used in the preparation of $\text{NaTi}_2(\text{PO}_4)_3/\text{C}$ electrode was PTFE. The mass ratio of active material, carbon black, and binder was 9:0.5:0.5. Moreover, when preparing the $\text{NaTi}_2(\text{PO}_4)_3/\text{C}$ electrode, titanium mesh, rather than carbon paper, was used as the current collector. A rolling machine (MSK-2150, KEJING) was used to compress the slurry on the mesh before the heat treatment.

2.5. Electrochemical and Deionization Tests

All the electrochemical and desalination tests were conducted with the electrochemical workstation (Multi autolab/M204, Metrohm). Galvanostatic charge–discharge (GCD) tests were used to measure the specific capacities of the electrode materials according to Equation (1):

$$C_s = \frac{I \times t}{3.6 \times m}, \quad (1)$$

in which C_s ($\text{mAh}\cdot\text{g}^{-1}$) is the specific capacity of the material, I (A) refers to the constant current intensity, t (s) denotes the discharging time in the test, and m (g) represents the mass of the active material in the electrode. Besides, the corresponding coulombic efficiency (η) was calculated as follows:

$$\eta = \frac{C_{\text{charge}}}{C_{\text{discharge}}} \quad (2)$$

where C_{charge} is the charge capacity and $C_{\text{discharge}}$ stands for the discharge capacity. Furthermore, the redox behaviors of the electrode materials were investigated with the cyclic voltammetry method in a 3-electrode system with Ag/AgCl as the reference electrode and platinum as the counter electrode, which was also employed in the GCD test to measure the electrochemical capacity of certain electrode material. In addition, the salt removal capacity (SAC, $\text{mg}\cdot\text{g}^{-1}$) in the desalination test was calculated as Equation (3):

$$\text{SAC} = \frac{(C_f - C_0) \times V}{M}, \quad (3)$$

in which C_f ($\text{mg}\cdot\text{L}^{-1}$) and C_0 ($\text{mg}\cdot\text{L}^{-1}$) are the final and initial salt concentrations of the feed solution during the deionization test, V (L) represents the volume of the saline solution, and M (g) stands for the total mass of the active materials in the CDI electrodes. The concentrations of chloride ions were measured with ion chromatography (883 Basic IC

Plus, Metrohm) and the CDI device was charged with the electrochemical workstation. Moreover, the salt removal rate ($SAR, \text{mg} \cdot \text{g}^{-1} \cdot \text{min}^{-1}$) was calculated as follows:

$$SAR = \frac{SAC}{T} \quad (4)$$

where T denotes the CDI reaction time (min). Additionally, the pH variations during the desalination tests were measured with a pH meter ((PHSJ-3F, Leica).

3. Results and Discussion

3.1. Characterization

The structure of $\text{LiMn}_2\text{O}_4/\text{C}$ is shown in Figure 1a,b. The nano-sized spinel LMO particles were surrounded by carbon spheres, which enhanced the charge transfer. Other structural information on $\text{LiMn}_2\text{O}_4/\text{C}$ could be acquired in our published article [25]. As shown in Figure 1c–f, rectangular $\text{NaTi}_2(\text{PO}_4)_3/\text{C}$ particles (200–300 nm) are agglomerated and the elements are homogeneously dispersed. The TEM images (Figure 1g–i) show clearer crystal structures of the $\text{NaTi}_2(\text{PO}_4)_3/\text{C}$ particle and the obvious carbon coating layer of about 5 nm, which could offer a charge transfer facility and crystal protection. According to the infrared carbon and sulfur analyzer, $\text{NaTi}_2(\text{PO}_4)_3/\text{C}$ had a carbon content of 3.11%.

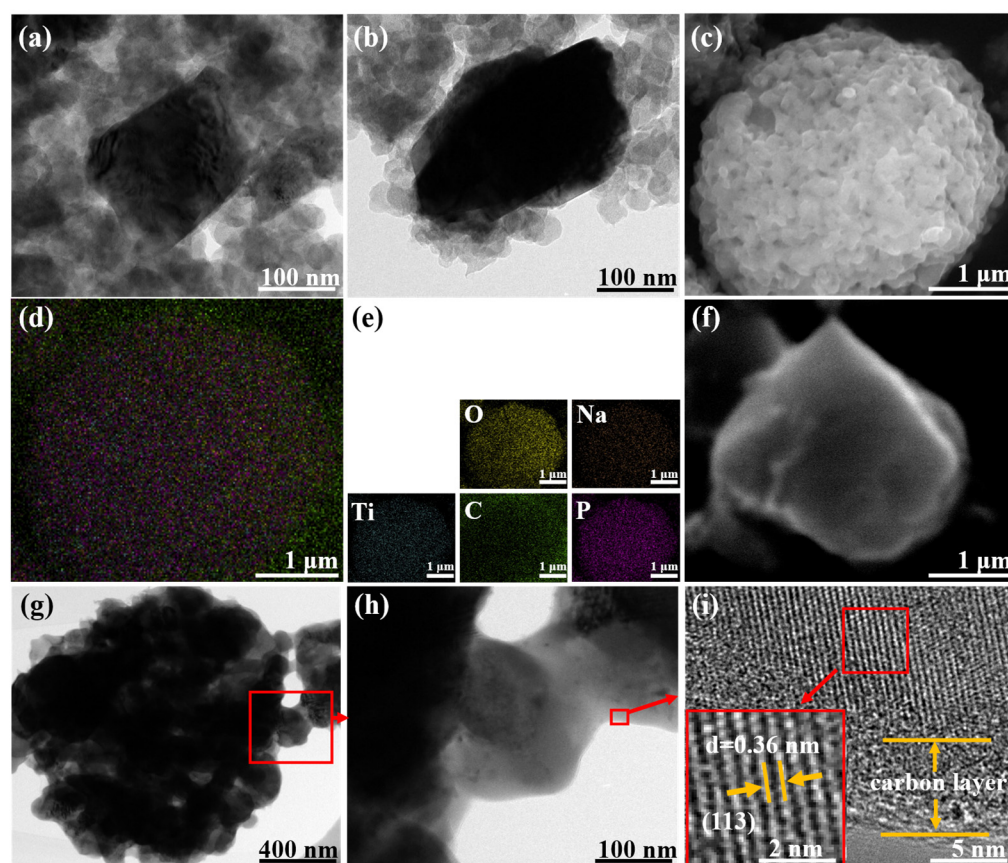


Figure 1. (a,b) TEM images of $\text{LiMn}_2\text{O}_4/\text{C}$ material; (c,f) SEM and (d,e) EDS images of $\text{NaTi}_2(\text{PO}_4)_3/\text{C}$ material; (g–i) TEM images of $\text{NaTi}_2(\text{PO}_4)_3/\text{C}$.

The BET results of prepared $\text{NaTi}_2(\text{PO}_4)_3/\text{C}$ are shown in Figure 2a,b. The material had a specific surface area of $10.23 \text{ m}^2 \cdot \text{g}^{-1}$, and the pore sizes were mainly distributed in the range of 5–30 nm. The XRD pattern of the anode material is presented in Figure 2c, which fits well with the standard pattern (JCPDS NO.33-1296), implying the successful synthesis of $\text{NaTi}_2(\text{PO}_4)_3/\text{C}$.

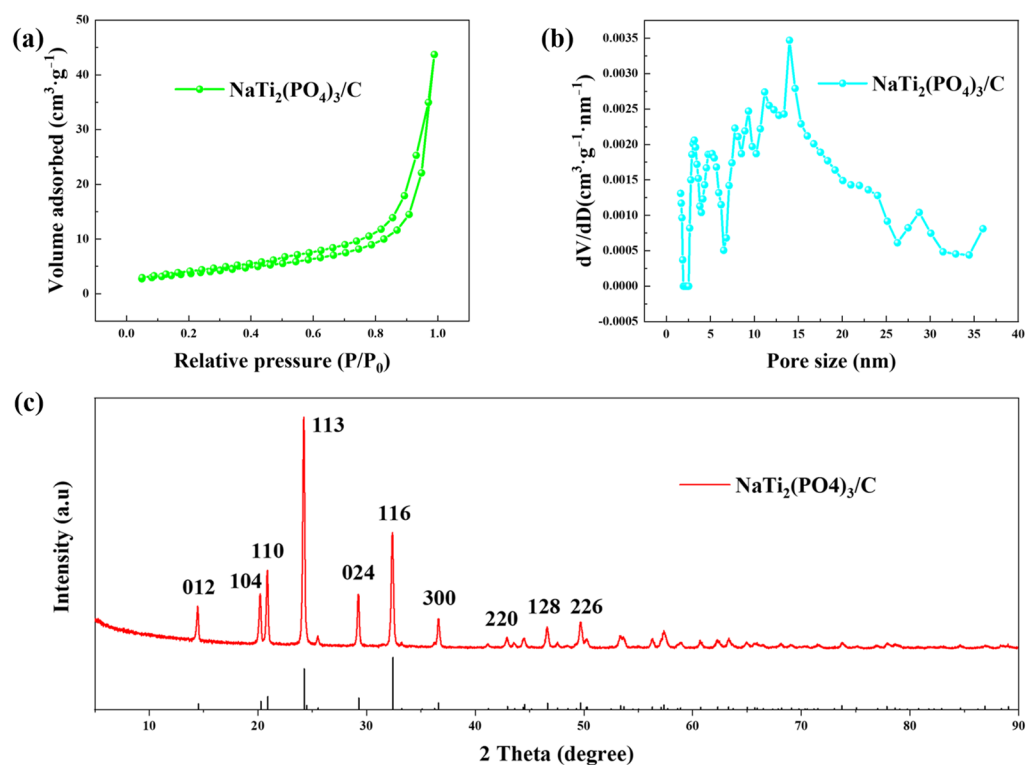


Figure 2. The (a) N_2 adsorption-desorption isotherm, (b) pore size distribution, and (c) XRD pattern of $NaTi_2(PO_4)_3/C$.

3.2. Electrochemical Tests

In the hybrid CDI system, AC is the most employed counter electrode of the battery electrode [31–33]. In this study, we employed the $NaTi_2(PO_4)_3/C$ composites with the sodium ion intercalation behavior to replace AC. Electrochemical tests were carried out to study the potential differences between the two materials as CDI electrodes.

As shown in Figure 3a, the electrochemical plateaus of the AC electrode during the GCD test with a low voltage range ($-1.0\sim 0$ V versus Ag/AgCl) were evidently asymmetrical, indicating severe hydrogen evolution, which was also verified by the cyclic voltammetry curve (Figure S1a). Nevertheless, hydrogen evolution was suppressed for $NaTi_2(PO_4)_3/C$ as reversible charging and discharging plateaus were observed in the GCD profile (Figure 3d), which was due to the intercalation/deintercalation reactions of sodium ions [34]. The cyclic voltammetry curve of $NaTi_2(PO_4)_3/C$ in Figure 3b exhibits reversible redox peaks signifying the release and capture of sodium ions, and no obvious hydrogen evolution peak was observed within the scan range, further indicating the alleviation of hydrogen evolution.

Reversible charging and discharging behaviors of $NaTi_2(PO_4)_3/C$ are clear in the GCD profile and a specific electrochemical capacity of $98.63\text{ mAh}\cdot\text{g}^{-1}$ was performed, 272.61% higher than that of AC ($26.47\text{ mAh}\cdot\text{g}^{-1}$, Figure S1b). The high capacity of the $NaTi_2(PO_4)_3/C$ anode was favorable for the full use of the capacity of the $LiMn_2O_4/C$ cathode ($70.57\text{ mAh}\cdot\text{g}^{-1}$, Figure S2a) in CDI desalination. On the other hand, as the anode acted as the counter electrode to the $LiMn_2O_4/C$ cathode and the reference electrode simultaneously in CDI, a GCD test of the $LiMn_2O_4/C$ - $NaTi_2(PO_4)_3/C$ couple was performed (Figure 3e). The GCD curve of the novel dual-ion electrode couple has a larger voltage window of 1.8 V, compared to that of the GCD curve in the two-electrode system with AC as the anode (1.0 V, Figure 3c). This was owing to the suppression of the hydrogen evolution reaction and the low potential of Ti^{4+}/Ti^{3+} (-0.8 V versus Ag/AgCl). The GCD test of $LiMn_2O_4/C$ - $NaTi_2(PO_4)_3/C$ was performed in a LiCl/NaCl mixed solution with 0.5 M as the concentrations of both solvents. No ion-exchange membrane was introduced into the

two-electrode cell for the convenience of comparison with GCD tests with other electrodes. Additionally, the sodium ion could rarely be intercalated into $\text{LiMn}_2\text{O}_4/\text{C}$ (Figure S2b) due to the larger ion radius (0.102 nm) compared to that of the lithium ion (0.076 nm) [35,36]. Hence, the mixed solution was chosen as the electrolyte in the capacity test of the novel electrode couple. Though the sodium ions seemed to be worse charge carriers in the GCD test than the lithium ions [37,38], the capacity of the $\text{LiMn}_2\text{O}_4/\text{C}-\text{NaTi}_2(\text{PO}_4)_3/\text{C}$ system with mixed electrolyte ($64.43 \text{ mAh}\cdot\text{g}^{-1}$) was 28.37% higher than that of the $\text{LiMn}_2\text{O}_4/\text{C}-\text{AC}$ system with pure LiCl electrolyte ($50.19 \text{ mAh}\cdot\text{g}^{-1}$), revealing a robust potential of enhancing desalination performance.

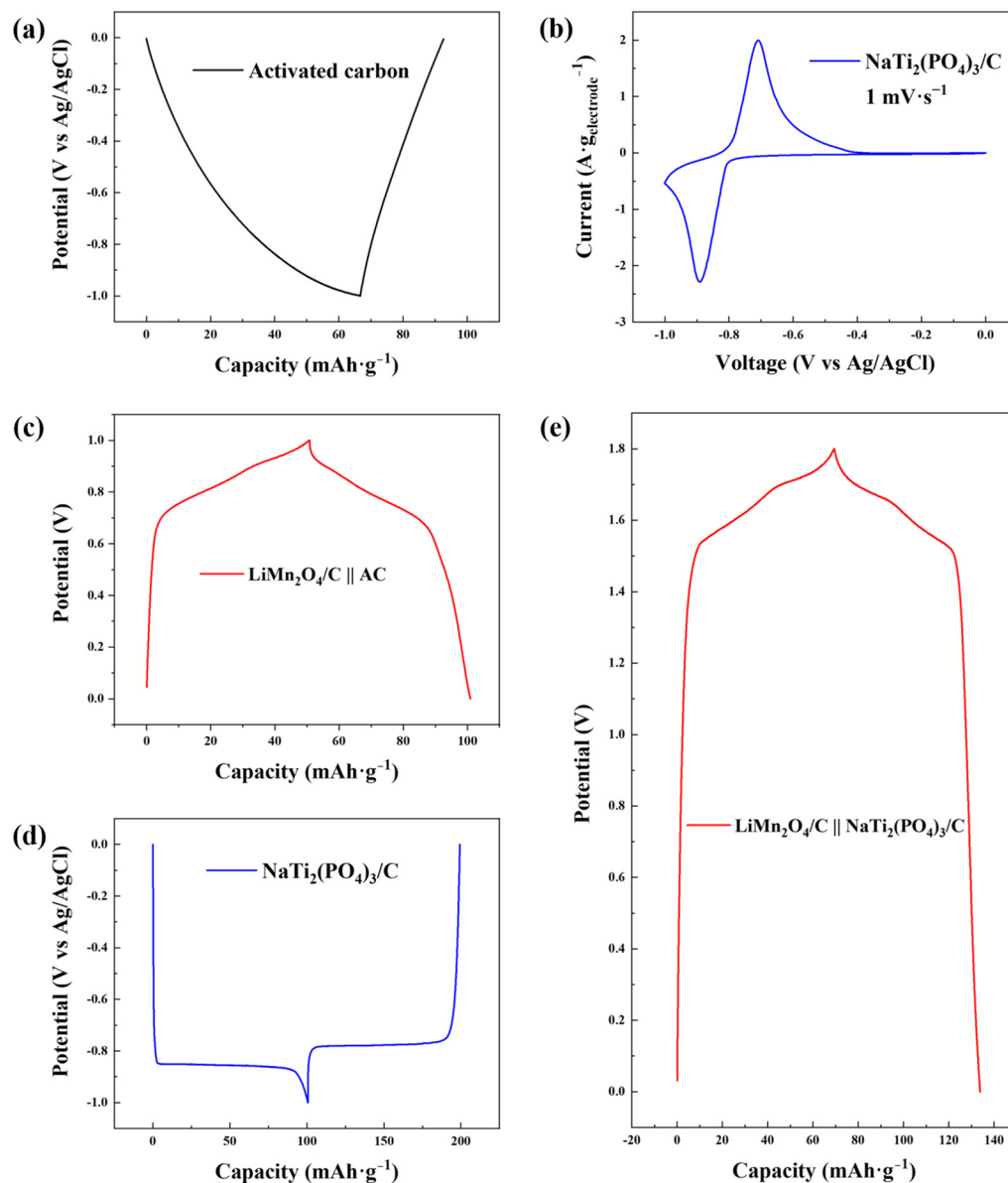


Figure 3. (a) GCD profile of AC in 1.0 M NaCl solution with the current density of $-0.1 \text{ A}\cdot\text{g}^{-1}$ with Ag/AgCl as the reference electrode; (b) cyclic voltammogram curve of $\text{NaTi}_2(\text{PO}_4)_3/\text{C}$ in 1.0 M NaCl solution with the scan rate of $1 \text{ mV}\cdot\text{s}^{-1}$; (c) GCD profile of $\text{LiMn}_2\text{O}_4/\text{C}$ in 1.0 M LiCl solution at the current density of $0.1 \text{ A}\cdot\text{g}^{-1}$ with AC as the counter electrode in the two-electrode system; (d) GCD profile of $\text{NaTi}_2(\text{PO}_4)_3/\text{C}$ in 1.0 M NaCl solution at the current density of $-0.1 \text{ A}\cdot\text{g}^{-1}$ with Ag/AgCl as the reference electrode; (e) GCD profile of $\text{LiMn}_2\text{O}_4/\text{C}$ in a mixed solution (0.5 M LiCl + 0.5 M NaCl) at the current density of $0.1 \text{ A}\cdot\text{g}^{-1}$ with $\text{NaTi}_2(\text{PO}_4)_3/\text{C}$ as the counter electrode in the two-electrode system.

3.3. Desalination Performance

The desalination test was conducted with the mode of constant voltage (CV) at room temperature in a CDI device, as shown in Figure 4a. The cell was divided by an anion-exchange membrane into two regions: the cathodic region with $\text{LiMn}_2\text{O}_4/\text{C}$ composites as the cathode and 10 mM LiCl solution (100 mL) as the catholyte, and the anodic region with $\text{NaTi}_2(\text{PO}_4)_3/\text{C}$ composites as the anode and NaCl solution (125 mL) as the feed solution. In addition, the total mass of the active materials in the cell was approximately 100 mg, with a mass ratio of about 1:1 for the cathode and anode. When a voltage was applied to the cathode, the lithium ions could be released from $\text{LiMn}_2\text{O}_4/\text{C}$ and attract the chloride ions from the other side of the membrane, and the sodium ions could be intercalated into $\text{NaTi}_2(\text{PO}_4)_3/\text{C}$ simultaneously, finishing the desalination of the feed solution.

Owing to the inhibition of hydrogen evolution at the $\text{NaTi}_2(\text{PO}_4)_3/\text{C}$ electrode, the cell could be applied by a high voltage during CDI desalination. The device was charged with different voltages and the reaction time was 4 h with an initial salt concentration of 10 mM. The corresponding desalination performances are shown in Figure 4b, from which we could figure out that 1.8 V was the appropriate voltage for high desalination performance with a deionization capacity of $122.79 \text{ mg}\cdot\text{g}^{-1}$. Basically, the salt removal capacity rose as the voltage increased, and 1.5 V brought out the lowest desalination capacity of $46.51 \text{ mg}\cdot\text{g}^{-1}$. This was owing to the fact that the higher voltage could provide a stronger electric field that facilitated ion transfer. However, it was also interesting that 1.8 V instead of 1.9 V was the applied voltage with the highest desalination performance at 10 mM, which was probably due to that more side reactions occurred at 1.9 V. The CDI cell was a two-electrode system with $\text{NaTi}_2(\text{PO}_4)_3/\text{C}$ electrode as the reference electrode, and the potential of the redox couple $\text{Ti}^{4+}/\text{Ti}^{3+}$ was about 0.8 V lower than the Ag/AgCl electrode, as shown in Figure 3d. Therefore, the voltage 1.9 V denotes an approximately 1.1 V versus Ag/AgCl applied to the $\text{LiMn}_2\text{O}_4/\text{C}$ electrode. In addition, the Ag/AgCl electrode potential is approximately 0.2 V higher than the standard hydrogen electrode, revealing that the 1.9 V applied to the desalination device was close to a voltage that was 0.1 V higher than the theoretical oxygen evolution potential. Thus, less oxygen evolution was performed at the applied voltage of 1.8 V, and a higher desalination efficiency could be obtained. Furthermore, the pH values in the solutions during desalination remained steady. Figure 4c depicts the salt removal rates at different voltages, and the voltage of 1.8 V was beneficial for fast desalination. The desalination rate of the whole CDI process in the dual-ion system reached $0.51 \text{ mg}\cdot\text{g}^{-1}\cdot\text{min}^{-1}$, over seven times that of the HCEDI cell with an AC anode [25].

The deionization capacities with different initial feed salinities at 1.8 V are shown in Figure 4d. An ultrahigh desalination capacity of $140.03 \text{ mg}\cdot\text{g}^{-1}$ was achieved with the initial salt concentration of 20 mM. The deionization performance was higher as the salt concentration went higher, which was likely because higher salinity offered higher conductivity and more ions for electrochemical capture. The salt removal capacities of other electrode couples in the literature are listed in Table 1, with which a clear comparison of desalination performances is revealed.

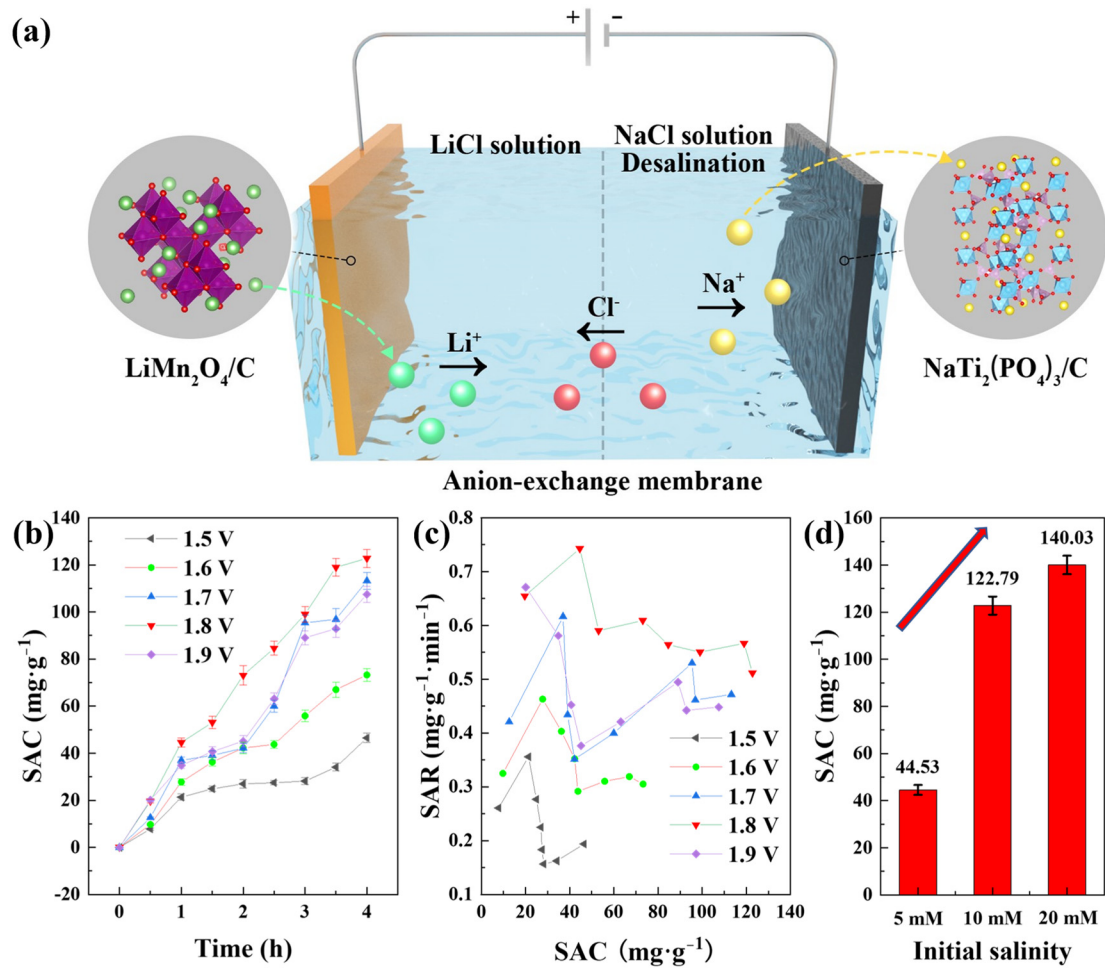


Figure 4. (a) The configuration of the CDI cell with dual-ion battery electrodes; (b) the deionization capacities of different voltages in the dual-ion desalination cell with the initial salinity of 10 mM; (c) the corresponding salt removal rates; (d) the desalination capacities with different initial salt concentrations.

Table 1. A comparison of the desalination performances of electrode couples in the literature and our work.

Electrode Couple	Charging Mode	Electric Intensity	Initial Salinity	CDI Capacity	Ref.
CNT CNT	CV	1.2 V	3500 ppm	$9.35 \text{ mg}\cdot\text{g}^{-1}$	[39]
porous carbon porous carbon	CV	1.2 V	292 ppm	$12.63 \text{ mg}\cdot\text{g}^{-1}$	[16]
MoS_2 AC	CV	1.2 V	400 mM	$8.81 \text{ mg}\cdot\text{g}^{-1}$	[40]
$\text{Na}_4\text{Mn}_9\text{O}_{18}$ AC	CV	1.2 V	50 mM	$31.2 \text{ mg}\cdot\text{g}^{-1}$	[20]
$\text{NaNiFe}(\text{CN})_6$ $\text{Na}_2\text{NiFe}(\text{CN})_6$	constant current (CC)	$0.28 \text{ mA}\cdot\text{cm}^{-2}$	20 mM	$34 \text{ mg}\cdot\text{g}^{-1}$	[41]
$\text{Na}_4\text{Ti}_9\text{O}_{20}/\text{C}$ AC	CV	1.4 V	1000 ppm	$66.14 \text{ mg}\cdot\text{g}^{-1}$	[22]
$\text{Na}_{0.71}\text{CoO}_2$ Ag/rGO	CV	1.4 V	500 ppm	$31 \text{ mg}\cdot\text{g}^{-1}$	[42]
$\text{Fe}_4[\text{Fe}(\text{CN})_6]_3/\text{rGO}$ rGO	CC	$0.1 \text{ A}\cdot\text{g}^{-1}$	2500 ppm	$80 \text{ mg}\cdot\text{g}^{-1}$	[43]
AC Bi	CV	1.2 V	500 ppm	$55.52 \text{ mg}\cdot\text{g}^{-1}$	[44]
$\text{Mo}_{1.33}\text{C-MXene}/\text{CNT}$ $\text{Mo}_{1.33}\text{C-MXene}/\text{CNT}$	CV	0.8 V	600 mM	$15 \text{ mg}\cdot\text{g}^{-1}$	[45]
polypyrrole/C polypyrrole/C	CV	1.2 V	500 ppm	$34.03 \text{ mg}\cdot\text{g}^{-1}$	[46]
MnO_2/C MnO_2/C	CV	1.2 V	500 ppm	$30.86 \text{ mg}\cdot\text{g}^{-1}$	[47]
$\text{Na}_3\text{V}_2(\text{PO}_4)_3/\text{C}$ AgCl	CC	$0.1 \text{ A}\cdot\text{g}^{-1}$	1000 ppm	$98.0 \text{ mg}\cdot\text{g}^{-1}$	[48]
Ag AgCl	CC	$1 \text{ mA}\cdot\text{cm}^{-2}$	500 mM	$85 \text{ mg}\cdot\text{g}^{-1}$	[22]
$\text{LiMn}_2\text{O}_4/\text{C}$ AC	CV	1.0 V	20 mM	$117.3 \text{ mg}\cdot\text{g}^{-1}$	[25]
$\text{LiMn}_2\text{O}_4/\text{C}$ $\text{NaTi}_2(\text{PO}_4)_3/\text{C}$	CV	1.8 V	20 mM	$140.03 \text{ mg}\cdot\text{g}^{-1}$	this work

The cycling performances of both electrodes in the CDI cell are presented in Figure 5. The capacities kept stable over the cycles, indicating the good cycling ability of the deionization device.

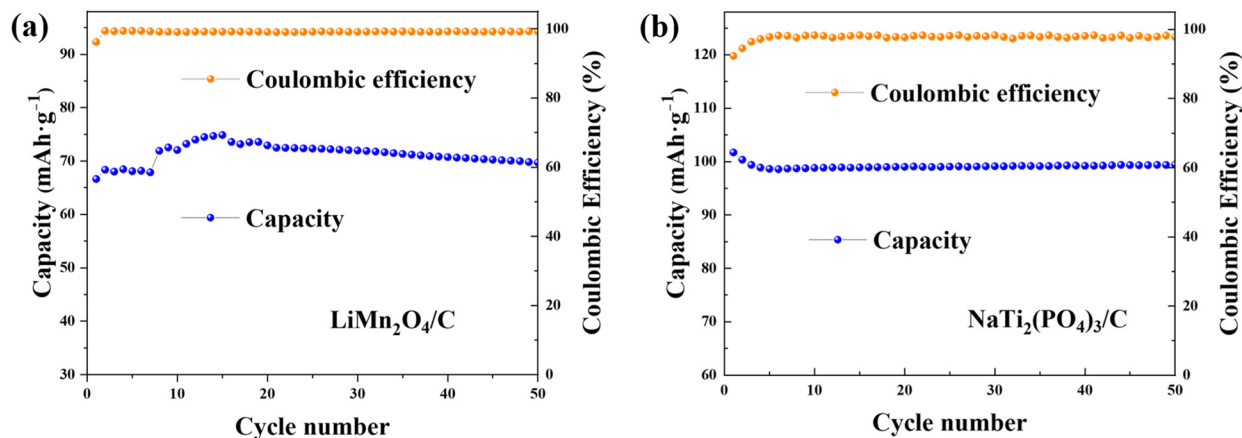


Figure 5. The cycling profiles of (a) $\text{LiMn}_2\text{O}_4/\text{C}$ in 1.0 M LiCl solution and (b) $\text{NaTi}_2(\text{PO}_4)_3/\text{C}$ with the constant current density of $0.1 \text{ g}\cdot\text{A}^{-1}$.

XRD (Figure 6) and XPS (Figure 7) tests were carried out to further study the variations of structures and valences in the electrode materials after desalination. The XRD peaks of $\text{LiMn}_2\text{O}_4/\text{C}$ shifted rightwards after the deionization test, signifying the release of lithium ions during charging. However, there were no evident peak shifts for the anode after CDI, which was due to the tiny structure conversion of $\text{NaTi}_2(\text{PO}_4)_3/\text{C}$ during the electrochemical reaction, which resulted from the strong covalent bonds in the polyanion tetrahedrons of the crystal structures [49].

As shown in Figure 7a, the amount ratio of Mn^{3+} (641.5 eV) and Mn^{4+} (642.7 eV) [50] was approximately 1:1 in pristine $\text{LiMn}_2\text{O}_4/\text{C}$, which was a key characteristic of the LiMn_2O_4 material. After desalination, the amount of Mn^{4+} was increased to over 90%, indicating the intense oxidation of manganese ions within the charging process. As for $\text{NaTi}_2(\text{PO}_4)_3/\text{C}$ before desalination, the two diffraction peaks (459.2 eV and 465.1 eV) fitted well with Ti^{4+} 2p, demonstrating the valence of titanium in $\text{NaTi}_2(\text{PO}_4)_3/\text{C}$ was +4. After the CDI process, another two peaks showed up (Ti^{3+} 2p_{1/2}: 464.1 eV, Ti^{3+} 2p_{1/2}: 457.9 eV) [51], implying the presence of Mn^{3+} . Thus, manganese and titanium were oxidated and reduced during the CDI process, respectively.

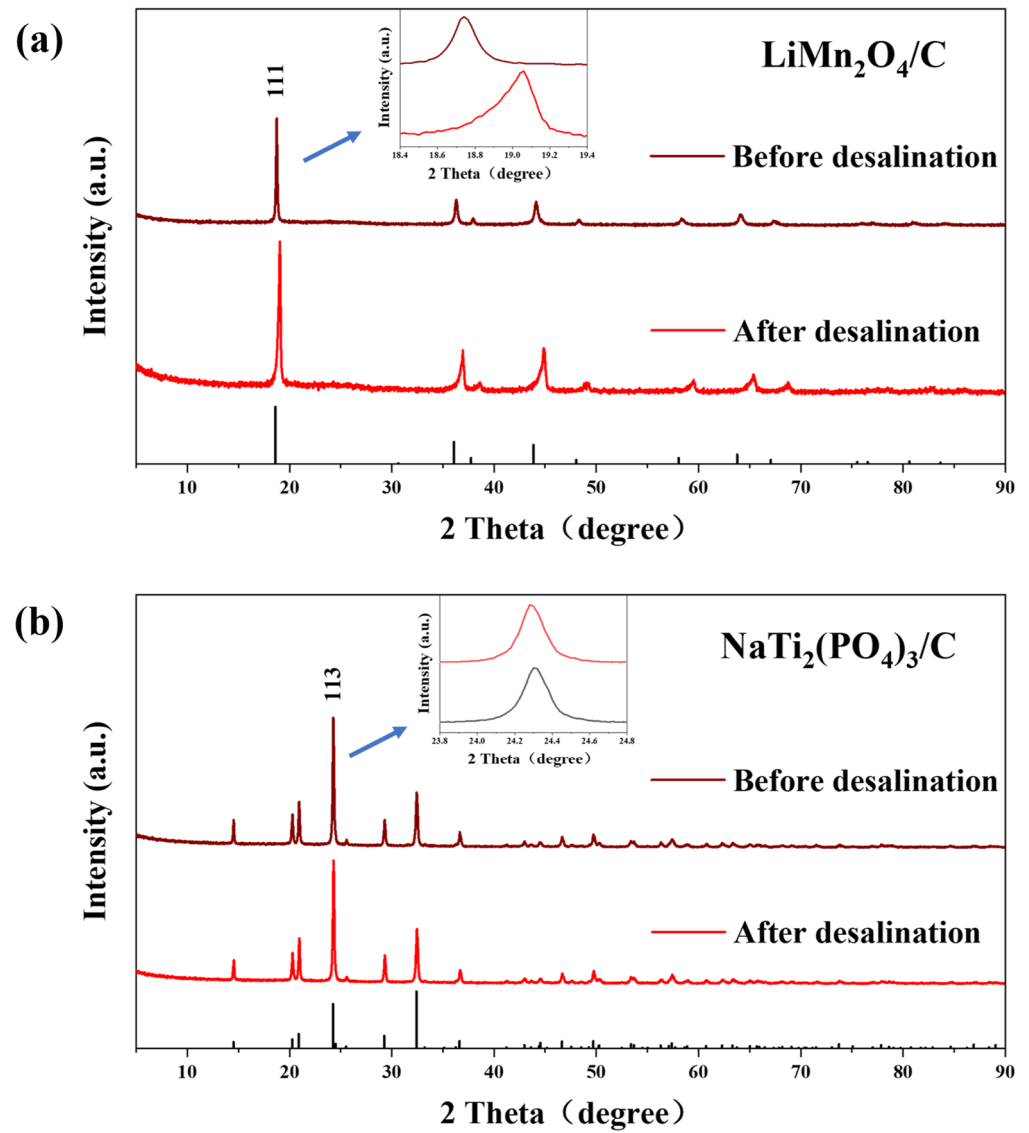


Figure 6. The (a) XRD patterns of $\text{LiMn}_2\text{O}_4/\text{C}$ and (b) $\text{NaTi}_2(\text{PO}_4)_3/\text{C}$ before and after the desalination test at 1.8 V in 10 mM salt solution.

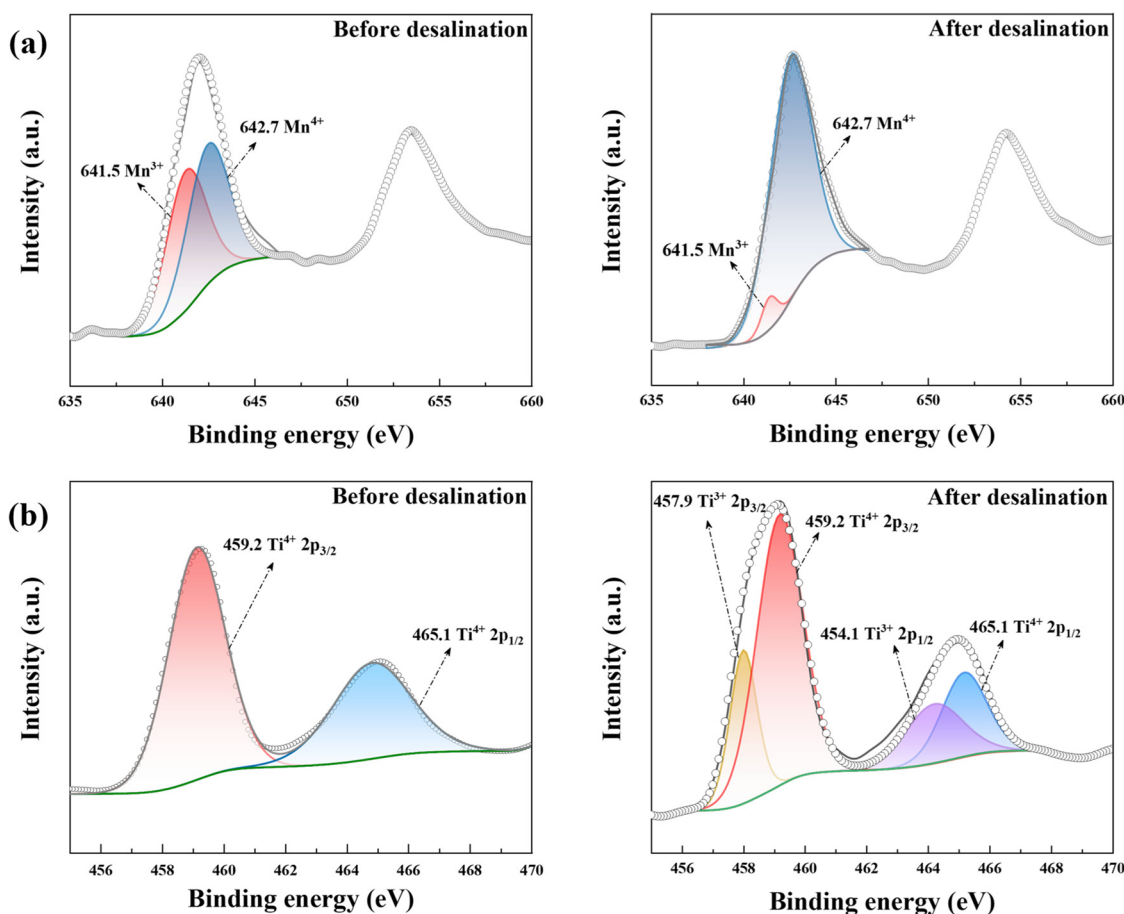


Figure 7. The XPS results of (a) Mn 2p in LiMn₂O₄/C and (b) Ti 2p in NaTi₂(PO₄)₃/C before and after the desalination test at 1.8 V in 10 mM salt solution.

4. Conclusions

In conclusion, a novel dual-ion CDI system with lithium-ion battery cathode LiMn₂O₄/C and sodium-ion battery anode NaTi₂(PO₄)₃/C was reported, which delivered an ultrahigh desalination capacity of 140.03 mg·g⁻¹ with the initial salinity of 20 mM. With the low potential of the redox couple Ti³⁺/Ti⁴⁺ and the alleviated hydrogen evolution during CDI desalination, the voltage window of CDI in the new cell could be enlarged to 1.8 V. Besides, after coupling with NaTi₂(PO₄)₃/C anode, the capacity of the LiMn₂O₄/C cathode was made full advantage of. The choice of the novel battery electrode couple resulted in an outstanding deionization performance, indicating a promising direction for future CDI desalination.

Supplementary Materials: The following supporting information can be downloaded at: <https://www.mdpi.com/article/10.3390/polym14214776/s1>, Figure S1. (a) Cyclic voltammetry profiles of activated carbon with different scan ranges and (b) the galvanostatic charge-discharge (GCD) curve of activated carbon (−0.3–0.7 V versus Ag/AgCl) with a current density of 0.1 A·g⁻¹ in 1.0 M NaCl solution; Figure S2. GCD curves of LiMn₂O₄/C (0.1 A·g⁻¹) in (a) 1.0 M LiCl solution and (b) 1.0 M NaCl solution; Figure S3. The concentration variations of lithium ions near the cathode and chloride ions in the feed solution during CDI desalination at 1.8 V with the initial salt concentration of 10 mM.

Author Contributions: Conceptualization, Y.J. and H.W.; methodology, Y.J.; software, L.Y.; validation, H.G.; formal analysis, Y.J.; investigation, Z.H.; resources, Y.J.; data curation, Z.H.; writing—original draft preparation, Y.J.; writing—review and editing, H.W.; visualization, L.Y.; supervision, L.C.; project administration, H.W.; funding acquisition, H.W. All authors have read and agreed to the published version of the manuscript.

Funding: This research was supported by the National Key Research and Development Program of China (2020YFC1909200).

Institutional Review Board Statement: Not applicable.

Conflicts of Interest: The authors declare no conflict of interest.

References

1. Liu, X.H.; Mishra, D.D.; Wang, X.B.; Peng, H.Y.; Hu, C.Q. Towards highly efficient solar-driven interfacial evaporation for desalination. *J. Mater. Chem. A* **2020**, *8*, 17907–17937. [[CrossRef](#)]
2. Hmtshirazi, R.; Mohammadi, T.; Asadi, A.A.; Tofighy, M.A. Electrospun nanofiber affinity membranes for water treatment applications: A review. *J. Water Process Eng.* **2022**, *47*, 102795. [[CrossRef](#)]
3. Prajapati, M.; Shah, M.; Soni, B. A review of geothermal integrated desalination: A sustainable solution to overcome potential freshwater shortages. *J. Clean. Prod.* **2021**, *326*, 129412. [[CrossRef](#)]
4. Ihsanullah, I.; Atieh, M.A.; Sajid, M.; Nazal, M.K. Desalination and environment: A critical analysis of impacts, mitigation strategies, and greener desalination technologies. *Sci. Total Environ.* **2021**, *780*, 146585. [[CrossRef](#)] [[PubMed](#)]
5. Yan, Z.S.; Qu, F.S.; Liang, H.; Yu, H.R.; Pang, H.L.; Rong, H.W.; Fan, G.D.; Van der Bruggen, B. Effect of biopolymers and humic substances on gypsum scaling and membrane wetting during membrane distillation. *J. Membr. Sci.* **2021**, *617*, 118638. [[CrossRef](#)]
6. Skuse, C.; Gallego-Schmid, A.; Azapagic, A.; Gorgojo, P. Can emerging membrane-based desalination technologies replace reverse osmosis? *Desalination* **2021**, *500*, 114844. [[CrossRef](#)]
7. Zhang, H.R.; He, Q.M.; Luo, J.Q.; Wan, Y.H.; Darling, S.B. Sharpening Nanofiltration: Strategies for Enhanced Membrane Selectivity. *ACS Appl. Mater. Interfaces* **2020**, *12*, 39948–39966. [[CrossRef](#)]
8. Nejati, S.; Mirbagheri, S.A.; Warsinger, D.M.; Fazeli, M. Biofouling in seawater reverse osmosis (SWRO): Impact of module geometry and mitigation with ultrafiltration. *J. Water Process Eng.* **2019**, *29*, 100782. [[CrossRef](#)]
9. Elimelech, M.; Phillip, W.A. The Future of Seawater Desalination: Energy, Technology, and the Environment. *Science* **2011**, *333*, 712–717. [[CrossRef](#)]
10. Porada, S.; Zhao, R.; van der Wal, A.; Presser, V.; Biesheuvel, P.M. Review on the science and technology of water desalination by capacitive deionization. *Prog. Mater. Sci.* **2013**, *58*, 1388–1442. [[CrossRef](#)]
11. Folaranmi, G.; Bechelany, M.; Sistas, P.; Cretin, M.; Zaviscka, F. Towards Electrochemical Water Desalination Techniques: A Review on Capacitive Deionization, Membrane Capacitive Deionization and Flow Capacitive Deionization. *Membranes* **2020**, *10*, 96. [[CrossRef](#)] [[PubMed](#)]
12. Al Radi, M.; Sayed, E.T.; Alawadhi, H.; Abdelkareem, M.A. Progress in energy recovery and graphene usage in capacitive deionization. *Crit. Rev. Environ. Sci. Technol.* **2021**, *52*, 3080–3136. [[CrossRef](#)]
13. Samimi, F.; Ghiyasiyan-Arani, M.; Salavati-Niasari, M. New avenue for preparation of potential hydrogen storage materials based on K10 montmorillonite and Ca₂Mn₃O₈/CaMn₃O₆ nanocomposites. *Fuel* **2022**, *320*, 123933. [[CrossRef](#)]
14. Liu, X.T.; Shanbhag, S.; Mauter, M.S. Understanding and mitigating performance decline in electrochemical deionization. *Curr. Opin. Chem. Eng.* **2019**, *25*, 67–74. [[CrossRef](#)]
15. Srimuk, P.; Su, X.; Yoon, J.; Aurbach, D.; Presser, V. Charge-transfer materials for electrochemical water desalination, ion separation and the recovery of elements. *Nat. Rev. Mater.* **2020**, *5*, 517–538. [[CrossRef](#)]
16. Baroud, T.N.; Giannelis, E.P. High salt capacity and high removal rate capacitive deionization enabled by hierarchical porous carbons. *Carbon* **2018**, *139*, 614–625. [[CrossRef](#)]
17. Li, Y.J.; Liu, Y.; Wang, M.; Xu, X.T.; Lu, T.; Sun, C.Q.; Pan, L.K. Phosphorus-doped 3D carbon nanofiber aerogels derived from bacterial-cellulose for highly-efficient capacitive deionization. *Carbon* **2018**, *130*, 377–383. [[CrossRef](#)]
18. Elisadiki, J.; King'ondo, C.K. Performance of ion intercalation materials in capacitive deionization/electrochemical deionization: A review. *J. Electroanal. Chem.* **2020**, *878*, 114588.
19. Li, Q.; Zheng, Y.; Xiao, D.J.; Or, T.; Gao, R.; Li, Z.Q.; Feng, M.; Shui, L.L.; Zhou, G.F.; Wang, X.; et al. Faradaic Electrodes Open a New Era for Capacitive Deionization. *Adv. Sci.* **2020**, *7*, 2002213. [[CrossRef](#)]
20. Lee, J.; Kim, S.; Kim, C.; Yoon, J. Hybrid capacitive deionization to enhance the desalination performance of capacitive techniques. *Energy Environ. Sci.* **2014**, *7*, 3683–3689. [[CrossRef](#)]
21. Ahn, J.; Lee, J.; Kim, S.; Kim, C.; Lee, J.; Biesheuvel, P.M.; Yoon, J. High performance electrochemical saline water desalination using silver and silver-chloride electrodes. *Desalination* **2020**, *476*, 114216. [[CrossRef](#)]
22. Yue, Z.S.; Gao, T.; Li, H.B. Robust synthesis of carbon@Na₄Ti₉O₂₀ core-shell nanotubes for hybrid capacitive deionization with enhanced performance. *Desalination* **2019**, *449*, 69–77. [[CrossRef](#)]
23. Tsujimoto, S.; Kondo, Y.; Yokoyama, Y.; Miyahara, Y.; Miyazaki, K.; Abe, T. Alkali Metal Ion Insertion and Extraction on Non-Graphitizable Carbon with Closed Pore Structures. *J. Electrochem. Soc.* **2021**, *168*, 070508. [[CrossRef](#)]
24. Hong, S.Y.; Kim, Y.; Park, Y.; Choi, A.; Choi, N.S.; Lee, K.T. Charge carriers in rechargeable batteries: Na ions vs. Li ions. *Energy Environ. Sci.* **2013**, *6*, 2067–2081. [[CrossRef](#)]
25. Jiang, Y.; Chai, L.; Zhang, D.; Ouyang, F.; Zhou, X.; Alhassan, S.I.; Liu, S.; He, Y.; Yan, L.; Wang, H.; et al. Facet-Controlled LiMn₂O₄/C as Deionization Electrode with Enhanced Stability and High Desalination Performance. *Nano-Micro Lett.* **2022**, *14*, 176. [[CrossRef](#)]

26. Ghiyasiyan-Arani, M.; Salayati-Niasari, M. Effect of $\text{Li}_2\text{CoMn}_3\text{O}_8$ Nanostructures Synthesized by a Combustion Method on Montmorillonite K10 as a Potential Hydrogen Storage Material. *J. Phys. Chem. C* **2018**, *122*, 16498–16509. [[CrossRef](#)]
27. Ghiyasiyan-Arani, M.; Salavati-Niasari, M. Synergic and coupling effect between SnO_2 nanoparticles and hierarchical AlV_3O_9 microspheres toward emerging electrode materials for lithium-ion battery devices. *Inorg. Chem. Front.* **2021**, *8*, 2735–2748. [[CrossRef](#)]
28. Wu, M.G.; Ni, W.; Hu, J.; Ma, J.M. NASICON-Structured $\text{NaTi}_2(\text{PO}_4)_3$ for Sustainable Energy Storage. *Nano-Micro Lett.* **2019**, *11*, 44. [[CrossRef](#)]
29. Fu, L.; Xue, X.; Tang, Y.G.; Sun, D.; Xie, H.L.; Wang, H.Y. Size controlling and surface engineering enable $\text{NaTi}_2(\text{PO}_4)_3/\text{C}$ outstanding sodium storage properties. *Electrochim. Acta* **2018**, *289*, 21–28. [[CrossRef](#)]
30. Zhang, X.; Dong, M.; Xiong, Y.; Hou, Z.; Qian, Y. Aqueous Rechargeable Li^+/Na^+ Hybrid Ion Battery with High Energy Density and Long Cycle Life. *Small* **2020**, *16*, 2003585. [[CrossRef](#)]
31. Chen, Z.Q.; Xu, X.T.; Ding, Z.B.; Wang, K.; Sun, X.; Lu, T.; Konarova, M.; Eguchi, M.; Shapter, J.G.; Pan, L.K.; et al. Ti_3C_2 MXenes-derived $\text{NaTi}_2(\text{PO}_4)_3/\text{MXene}$ nanohybrid for fast and efficient hybrid capacitive deionization performance. *Chem. Eng. J.* **2021**, *407*, 127148. [[CrossRef](#)]
32. Srimuk, P.; Lee, J.; Tolosa, A.; Kim, C.; Aslan, M.; Presser, V. Titanium Disulfide: A Promising Low-Dimensional Electrode Material for Sodium Ion Intercalation for Seawater Desalination. *Chem. Mat.* **2017**, *29*, 9964–9973. [[CrossRef](#)]
33. Kim, S.; Lee, J.; Kim, C.; Yoon, J. $\text{Na}_2\text{FeP}_2\text{O}_7$ as a Novel Material for Hybrid Capacitive Deionization. *Electrochim. Acta* **2016**, *203*, 265–271. [[CrossRef](#)]
34. Tan, J.F.; Zhu, W.H.; Gui, Q.Y.; Li, Y.Y.; Liu, J.P. Weak Ionization Induced Interfacial Deposition and Transformation towards Fast-Charging $\text{NaTi}_2(\text{PO}_4)_3$ Nanowire Bundles for Advanced Aqueous Sodium-Ion Capacitors. *Adv. Funct. Mater.* **2021**, *31*, 2101027. [[CrossRef](#)]
35. Zhao, M.Y.; Ji, Z.Y.; Zhang, Y.G.; Guo, Z.Y.; Zhao, Y.Y.; Liu, J.; Yuan, J.S. Study on lithium extraction from brines based on $\text{LiMn}_2\text{O}_4/\text{Li}_{1-x}\text{Mn}_2\text{O}_4$ by electrochemical method. *Electrochim. Acta* **2017**, *252*, 350–361. [[CrossRef](#)]
36. Guerfi, A.; Trottier, J.; Gagnon, C.; Barray, F.; Zaghbi, K. High rechargeable sodium metal-conducting polymer batteries. *J. Power Source* **2016**, *335*, 131–137. [[CrossRef](#)]
37. Kubota, K.; Dahbi, M.; Hosaka, T.; Kumakura, S.; Komaba, S. Towards K-Ion and Na-Ion Batteries as “Beyond Li-Ion”. *Chem. Rec.* **2018**, *18*, 459–479. [[CrossRef](#)] [[PubMed](#)]
38. Natarajan, S.; Subramanyan, K.; Aravindan, V. Focus on Spinel $\text{Li}_4\text{Ti}_5\text{O}_{12}$ as Insertion Type Anode for High-Performance Na-Ion Batteries. *Small* **2019**, *15*, 1904484. [[CrossRef](#)] [[PubMed](#)]
39. Wang, S.; Wang, D.Z.; Ji, L.J.; Gong, Q.M.; Zhu, Y.F.; Liang, J. Equilibrium and kinetic studies on the removal of NaCl from aqueous solutions by electrosorption on carbon nanotube electrodes. *Sep. Purif. Technol.* **2007**, *58*, 12–16. [[CrossRef](#)]
40. Xing, F.; Li, T.; Li, J.Y.; Zhu, H.R.; Wang, N.; Cao, X. Chemically exfoliated MoS_2 for capacitive deionization of saline water. *Nano Energy* **2017**, *31*, 590–595. [[CrossRef](#)]
41. Porada, S.; Shrivastava, A.; Bukowska, P.; Biesheuvel, P.M.; Smith, K.C. Nickel Hexacyanoferrate Electrodes for Continuous Cation Intercalation Desalination of Brackish Water. *Electrochim. Acta* **2017**, *255*, 369–378. [[CrossRef](#)]
42. Liu, Z.Z.; Yue, Z.S.; Li, H.B. $\text{Na}_{0.71}\text{CoO}_2$ promoted sodium uptake via faradaic reaction for highly efficient capacitive deionization. *Sep. Purif. Technol.* **2020**, *234*, 116090. [[CrossRef](#)]
43. Vafakhah, S.; Guo, L.; Sriramulu, D.; Huang, S.; Saeedikhani, M.; Yang, H.Y. Efficient sodium-ion intercalation into the freestanding Prussian blue/graphene aerogel anode in a hybrid capacitive deionization system. *ACS Appl. Mater. Interfaces* **2019**, *11*, 5989–5998. [[CrossRef](#)] [[PubMed](#)]
44. Chang, J.J.; Duan, F.; Su, C.L.; Li, Y.P.; Cao, H.B. Removal of chloride ions using a bismuth electrode in capacitive deionization (CDI). *Environ. Sci. Wat. Res. Technol.* **2020**, *6*, 373–382. [[CrossRef](#)]
45. Srimuk, P.; Halim, J.; Lee, J.; Tao, Q.Z.; Rosen, J.; Presser, V. Two-Dimensional Molybdenum Carbide (MXene) with Divacancy Ordering for Brackish and Seawater Desalination via Cation and Anion Intercalation. *ACS Sustain. Chem. Eng.* **2018**, *6*, 3739–3747. [[CrossRef](#)]
46. Miao, L.W.; Wang, Z.; Peng, J.; Deng, W.Y.; Chen, W.Q.; Dai, Q.Z.; Ueyama, T. Pseudocapacitive deionization with polypyrrole grafted CMC carbon aerogel electrodes. *Sep. Purif. Technol.* **2022**, *296*, 121441. [[CrossRef](#)]
47. Li, Y.L.; Cai, Y.M.; Wang, Y.; Liu, D.X.; Guo, J.Q. A Study of 3D flake MnO_2 nanoflower decorated hollow carbon spheres as cathode material for pseudo-capacitive deionization. *J. Environ. Chem. Eng.* **2022**, *10*, 107266. [[CrossRef](#)]
48. Zhao, W.Y.; Guo, L.; Ding, M.; Huang, Y.X.; Yang, H.Y. Ultrahigh-Desalination-Capacity Dual-Ion Electrochemical Deionization Device Based on $\text{Na}_3\text{V}_2(\text{PO}_4)_3/\text{C}-\text{AgCl}$ Electrodes. *ACS Appl. Mater. Interfaces* **2018**, *10*, 40540–40548. [[CrossRef](#)]
49. Ahsan, M.T.; Ali, Z.; Usman, M.; Hou, Y.L. Unfolding the structural features of NASICON materials for sodium-ion full cells. *Carbon Energy* **2022**, *4*, 776–819. [[CrossRef](#)]
50. Yang, C.X.; Deng, Y.F.; Gao, M.; Yang, X.F.; Qin, X.S.; Chen, G.H. High-rate and long-life performance of a truncated spinel cathode material with off-stoichiometric composition at elevated temperature. *Electrochim. Acta* **2017**, *225*, 198–206. [[CrossRef](#)]
51. Liu, Z.X.; An, Y.F.; Pang, G.; Dong, S.Y.; Xu, C.Y.; Mi, C.H.; Zhang, X.G. TiN modified $\text{NaTi}_2(\text{PO}_4)_3$ as an anode material for aqueous sodium ion batteries. *Chem. Eng. J.* **2018**, *353*, 814–823. [[CrossRef](#)]